Article:

Tang, H. orcid.org/0000-0002-2924-0126, Hu, K. orcid.org/0000-0002-9988-5747, Huang, G. et al. (2 more authors) (2022) Intensification and Northward extension of Northwest Pacific anomalous anticyclone in El Niño decaying mid-summer: an energetic perspective. Climate Dynamics, 58 (1-2). pp. 591-606. ISSN 0930-7575

https://doi.org/10.1007/s00382-021-05923-5

Intensification and Northward Extension of Northwest Pacific Anomalous Anticyclone in El Niño Decaying Mid-Summer: An Energetic Perspective

Haosu Tang[1,3], Kaiming Hu[1,2], Gang Huang[1,2,3], Ya Wang[1,3] and Weichen Tao[1]

[1]State key Laboratory of Numerical Modeling for Atmospheric Sciences and Geophysical Fluid Dynamics and Center for Monsoon System Research, Institute of Atmospheric Physics, Chinese Academy of Sciences, Beijing, China

[2]Laboratory for Regional Oceanography and Numerical Modeling, Qingdao National Laboratory for Marine Science and Technology，Qingdao 266237，China

[3]University of Chinese Academy of Sciences, Beijing, 100049, China

Submitted to Climate Dynamics

*Corresponding authors: Kaiming Hu and Gang Huang

Corresponding author address: Kaiming Hu, IAP/CAS, P.O. Box 9804, Beijing 100029, China; E-mail: hkm@mail.iap.ac.cn and Gang Huang, IAP/CAS, P.O. Box 9804, Beijing 100029, China; E-mail: hg@mail.iap.ac.cn

Abstract

The Northwest Pacific (NWP) anomalous anticyclone (AAC) intensifies and extends northward from El Niño decaying early to mid- summer, despite decaying El Niño-induced sea surface temperature (SST) anomalies in the North Indian Ocean, North Atlantic and subtropical NWP. The present study suggests the intra-seasonal variations of AAC are induced by local mean state changes and investigates the underlying mechanisms from the perspective of energetics. Compared with early summer, the efficiency of dry energy conversion from the mean flow to El Niño-excited AAC pattern increases in El Niño decaying mid-summer. The moist feedback over subtropical NWP is also enhanced in El Niño decaying mid-summer due to the onset of the climatological NWP summer monsoon. Both of them contribute to the intensification of El Niño-excited AAC pattern. Moreover, mean state changes over East Asia–NWP from early to mid- summer are found in favor of the northward shift of the preferred latitude of the circulation anomalies. Thus, the El Niño-excited AAC pattern are more northward-extended in El Niño decaying mid-summer. Empirical orthogonal function analyses further confirm that the northward extension of El Niño-excited AAC pattern stems from changes of local internal dynamic mode. The present study highlights that both the El Niño-induced SST anomalies and local atmospheric internal dynamics are of paramount importance for the intra-seasonal variations of AAC in El Niño decaying summer.

Keywords El Niño; Anomalous anticyclone; Intra-seasonal variations; Dynamic mode

1. Introduction

Boreal summer is the major rainy season for East Asia (EA) and Northwest Pacific (NWP). The precipitation here over this period shows immense interannual variability, which is of great socioeconomic importance for the livelihood of over two billion inhabitants (Wang et al. 2001; Huang et al. 2007; Wei et al. 2020). El Niño-Southern Oscillation (ENSO) is the leading source for local rainfall variability via giving rise to an anomalous anticyclone (AAC) in the lower troposphere over the Indo-NWP region during El Niño decaying summer (Fu and Ye 1988; Zhang et al. 1996; Wang et al. 2003). As the tropical lobe of the Pacific–Japan (PJ) pattern (Nitta 1987) or the East Asia–Pacific (EAP) pattern (Huang and Wu 1989), the lower-level AAC appears in conjunction with an anomalous cyclone to its northeast during El Niño decaying summer. This El Niño-excited PJ pattern exerts far-reaching influence on the weather and climate over EA–NWP during El Niño decaying summer (Kosaka et al. 2013; Xie et al. 2016). For instance, the AAC can induce floods at its northern flank via moisture convergence (Huang and Wu 1989; Chang et al. 2000) and droughts in its ridge via subsidence motion (Wang et al. 2000). Besides, the AAC could lead to above-normal surface air temperature (SAT) anomalies in south China through reduced rainfall and downward vertical motion, while the anomalous cyclonic circulation to the north will bring about below-normal SAT anomalies in northeast China through upward vertical motion (Hu et al. 2011; Kim and Kug 2021). Furthermore, the AAC could decrease tropical cyclone geneses over major parts of the tropical NWP (Du et al. 2011).

As for the maintenance mechanisms of the summer AAC, El Niño-induced sea surface temperature (SST) anomalies in the tropical Indian Ocean, tropical Atlantic, and NWP are considered playing an important role. El Niño events generally mature in boreal winter with maximum SST warming in the equatorial eastern Pacific. In the following months, SST anomalies in the equatorial eastern Pacific decay rapidly, but the associated SST anomalies in the tropical Indian Ocean, tropical Atlantic, and NWP can maintain into summer via atmospheric bridge (Klein et al. 1999; Alexander et al.

2002), ocean dynamics (Xie et al. 2002; Huang and Kinter 2002) and air–sea interaction (Wang et al. 2000; Du et al. 2009; Kosaka et al. 2013; Xie et al. 2016). The warming in the tropical Indian Ocean and tropical North Atlantic can intensify the AAC via the lower-level Ekman divergence invoked by warm equatorial Kelvin wave response (Xie et al. 2009; Rong et al. 2010; Li et al. 2017), while the NWP cooling can intensify the AAC via the atmospheric descending Rossby wave response (Wang et al. 2000; Xiang et al. 2013).

The fundamental works of the last twenty years successfully explain the maintenance of AAC on the summer seasonal mean timescale, mainly focusing on the role of SST anomalies in three tropical oceans. Nevertheless, the AAC is not only a mode excited by anomalous SST forcing, but could also arise from the atmospheric internal dynamic processes unrelated to SST variability (Kosaka et al. 2013; Zhou et al. 2018; Wang et al. 2018; Wang et al. 2020; 2021). Hu et al. (2019) illustrated that the AAC could extract kinetic energy (*KE*) from background mean flow via barotropic energy conversion in the NWP confluence zone and emphasized the importance of the above process in amplifying the impact of SST anomalies on the AAC. However, the background mean flow over the EA–NWP changes dramatically from early to mid-summer. In that case, how will the AAC change correspondingly?

Previous studies reveal an intensification (Xiang et al. 2013) and northward extension (Ye and Lu 2010; Hu et al. 2017; Li and Lu 2018) of the AAC in El Niño decaying summer. As for its possible reason, Ye and Lu (2010) suggested the northward shift of the upper-level westerly jet and West Pacific Subtropical High (WPSH) is responsible for the northward extension of the AAC, which is confirmed by Kosaka and Nakamura (2010) where they conducted two numerical experiments with the westerly jet axis set at 35°N and 50°N, respectively. They found the circulation response is enhanced and displaced poleward in the later experiment. Although previous studies have successfully established the link between changes of background mean flow and the intra-seasonal variations of AAC, the underlying mechanism remains a knowledge gap: how the above two phenomena are dynamically linked? Thus, the concrete process of changes in wave–mean flow interactions over the EA–NWP during El Niño decaying summer entails further comprehension.

On the other hand, Xiang et al. (2013) emphasized the role of enhanced mean precipitation over the NWP in the intensification of the AAC via making atmospheric responses more sensitive to the external forcing (Wu et al. 2010). In the present study, we attempt to bring the above two lines of reasons to the theoretical framework developed by Kosaka and Nakamura (2010) and quantify the effect of local mean state changes on the intra-seasonal variations of AAC from the perspective of energetics. The remaining paper is structured as follows. Section 2 describes the data and methods. Section 3 displays the variations of ocean–atmosphere anomalies in each month of the El Niño decaying summer. The energy conversion/generation processes between EA–NWP background mean states and the El Niño-excited PJ pattern are diagnosed in section 4. Conclusion and discussions are given in section 5.

2. Data and methods

2.1 Datasets

In this study, the monthly and daily mean atmospheric variables are from the National Centers for the Environmental Prediction–Department of Energy (NCEP–DOE) atmospheric reanalysis, which have a horizontal resolution of 2.5°×2.5° at 17 height levels (Kanamitsu et al. 2002). Pentad-mean precipitation data is from the Climate Prediction Center (CPC) Merged Analysis of Precipitation (CMAP; Xie and Arkin 1997), given on a 2.5°×2.5° horizontal grid. The interpolated daily outgoing longwave radiation (OLR) data is from the National Oceanic and Atmospheric Administration (NOAA) (Liebmann and Smith 1996) and utilized as a proxy for convection, with 2.5° × 2.5° horizontal resolution. The global gridded monthly SST dataset is from the UK. Met Office Hadley Centre, with 1°×1° horizontal resolution (Rayner et al. 2003). The study period is from January 1979 to December 2016.

2.2 Methods

Since the present study focuses on the interannual variabilities associated with ENSO, the linear trend and 9-yr running mean are removed from all monthly and daily datasets to eliminate the long-term trend and decadal variability. The numeral 0 (1) in parentheses denotes the El Niño developing (decaying) years. The El Niño events are selected based on the 3-month running means of the detrended and standardized December(0)–February(1) [DJF(0)] Niño 3.4 index, which is defined as the mean SST anomalies averaged over the region 5°S–5°N and 170°W–120°W. An El Niño year is defined when the value is more than 0.75, consistent with Kong and Chiang (2020). Thus, seven El Niño events (namely, 1982/83, 1991/92, 1994/95, 1997/98, 2002/03, 2009/10 and 2015/16) are selected for further study. Note that the unconventional 1986 El Niño event is ruled out because it lasts for 2 yr and negative SST anomalies cover the Indian Ocean during its decaying summer (figure not shown). All the statistically significant tests for the composite and regression analyses are performed using the two-tailed Student's t test.

3. Variations of ocean-atmosphere anomalies in El Niño decaying summer

Figures 1 a, d, g show the composite monthly 850 hPa wind and SAT anomalies from climatological mean in each month of the El Niño decaying summer. The AAC pattern persists throughout the summer, while its spatial structure and amplitude experience pronounced changes. The northern flank of AAC marches northward from 25°N in June(1) to 35°N in July(1) and 37°N in August(1). Besides, the intensity of AAC is observed to increase from June(1) to July(1). The AAC intensity is defined as the maximum composite sea level pressure (SLP) anomalies around the NWP (10°–20°N, 110°–150°E), and is 81.925, 229.629 and 187.592 Pa in June(1), July(1) and August(1), respectively.

Since the moisture is mainly confined in the lower troposphere, the pattern of the composite vertically integrated moisture fluxes highly resembles the AAC pattern in each month of El Niño decaying summer (Figs. 1b, e, h). Both SAT and rainfall anomalies display a meridional dipole pattern over the EA–NWP, with positive SAT and negative rainfall anomalies in the ridge of the AAC and opposite anomalies at its northern flank. Accompanied with the intensification and northward extension of the AAC, the monthly SAT (Figs. 1 a, d, g) and rainfall (Figs. 1 b, e, h) anomalies over the EA–NWP also gradually march northward. Specific in China, negative (positive) SAT (rainfall) anomalies are observed around south China in June(1), while move to the mid-latitudes in July(1) and August(1) when the south China is occupied by positive (negative) SAT (rainfall) anomalies. These results indicate that the El Niño-excited circulation and climate anomalies over the EA–NWP have pronounced month-to-month variations during JJA(1) season.

Figures 1 c, f, i show the composite SST anomalies in each month of El Niño decaying summer. In June(1), there is prominent warming in the tropical North Atlantic (NA), North Indian Ocean (NIO), and cooling in the subtropical NWP. In July(1) and August(1), the warming in the tropical NA, NIO and cooling in the subtropical NWP all gradually decay. The SST anomalies averaged over the NA (0°–20°N, 60°W–20°W), NIO (5°–25°N, 40°E–100°E) and subtropical NWP (10°–20°N, 150°–170°E) from June(1) to August(1) are calculated. The values are 0.283 (0.326, -0.264), 0.271 (0.288, -0.089), 0.229 (0.229, -0.065) K for NA (NIO, NWP) in June(1), July(1) and August(1), respectively. The tropical anomalous SST pattern from west to east (Fig. 1c) is considered responsible for the long-lasting maintenance of the summer AAC (Xie et al. 2016; Li et al. 2017), while the decaying of such anomalous SST pattern from June(1) to August(1) could not account for the intensification of the AAC. Thus, other factors besides the El Niño-induced SST anomalies may contribute to the intensification of the AAC on the intra-seasonal timescale.

To further illustrate the intra-seasonal variations of AAC during El Niño decaying summer, daily datasets are used to pin down its evolution features. Figure 2 shows the meridional section of the composite pentad-mean precipitation, OLR, and 850 hPa wind anomalies averaged between 110°–150°E during El Niño decaying summer. The northern flank of AAC leaps from ~30°N in mid-June(1) to ~35°N in late July(1), coinciding well with the anomalous rainband. Note that the decaying of the AAC during late August(1) may be attributed to the negative feedback of positive SST anomalies on the atmosphere over the NWP (Lu et al. 2014). Figure 2 indicates that the intra-seasonal variations of the AAC do not accurately follow the calendar months, consistent with previous studies (Ye and Lu 2010; Hu et al. 2012). Thus, the summer is divided into two periods for further analysis. One is early summer (15 June–14 July), and the other is mid-summer (20 July–18 August), corresponding to the climatological EA and NWP rainy season, respectively (Kosaka et al. 2011).

Previous studies suggested that the decaying El Niño could intensify the climatological WPSH through inducing an AAC on the summer seasonal mean timescale (e.g., Xie et al. 2009). However, the climatological WPSH and AAC both experience dramatic intra-seasonal variations from early to mid- summer. Thus, the decaying El Niño's influence on the climatological WPSH in summer needs to be further unraveled. Figures 3 a, b, d, e show the climatological and El Niño–related anomalous 500 hPa winds and SLP in early and mid- summer, respectively. The climatological WPSH marches northward and retreats eastward from early to mid- summer (Figs. 3a, b), consistent with previous studies (e.g., Tao and Chen 1987). In El Niño decaying early summer (Fig. 3d), there are meridional dipole circulation anomalies over the EA–NWP relative to the climatology, with anticyclonic anomalies over the subtropical NWP and cyclonic anomalies over south Japan. While in El Niño decaying mid-summer (Fig. 3e), there are two anticyclonic centers. One is over eastern China, and the other is over the North Pacific around 40°N. Thus, we can divide the WPSH into two parts: 105°–140°E and 140°–170°E. In the longitudes 140°–170°E, the changes of El Niño–related anomalous winds from early to mid- summer (Fig. 3f) are generally in accordance with those in the climatological winds (Fig. 3c), suggesting the decaying El Niño could strengthen the climatological northward migration and intensification of WPSH over the North Pacific. In the longitudes 105°–140°E, although the El Niño–related AAC also shifts northward from early to mid-summer

(Fig. 3f), its phase lags the climatological northward migration of WPSH by about 10° latitude (Fig. 3c), indicating that the decaying El Niño may hinder the climatological northward migration of WPSH over eastern China and bring extended rainy season with decreased sunshine to the locality.

4. Energetic analyses

In this section, we first examine mean state changes over the EA–NWP from early to mid- summer, then compare the efficiency of energy conversions/generation from background mean states to the AAC between the two periods.

4.1 Mean state changes from early to mid- summer

Figures 4a, b present the climatological 850 hPa winds and precipitation. The lower-level winds over the NWP feature a confluence between the westerly monsoon winds from the NIO and easterly trade winds associated with WPSH. Accompanied with the advancement of the summer westerly monsoon, the confluence zone gradually shifts eastward until the NWP monsoon trough is completely established in mid-summer (Fig. 4b). As for precipitation, the withdrawal of mei–yu/baiu rainband and the emergence of the NWP rainband are observed in mid- summer, marking the onset of the climatological NWP summer monsoon (Zhou et al. 2016). Figures 4c, d show the climatological mean winds at 200 hPa and air temperature at 500 hPa. Accompanied with the northward shift of the solar radiation, high air temperature centers in the EA extend northward from early to mid- summer. The climatological upper-level westerly jet shifts northward from ~40°N in the early summer to ~48°N in mid-summer (Lin and Lu 2008). Besides, the exit of the westerly jet over Japan weakens in mid-summer.

Atmospheric circulation anomalies often organize themselves into certain preferred patterns, in which case they could most efficiently extract energy from background mean flows (Simmons et al. 1983; Branstator 1985) and these anomalies are called the dynamic modes (the most excitable unstable modes) in the atmosphere. The PJ pattern is the dynamic mode over the EA–NWP in the summer (Kosaka and Nakamura 2006; 2010; Hirota and Takahashi 2012), which is usually characterized by zonally-elongated horizontal pattern and northwestward tilting vertical structure (Xu et al. 2019; Zhu et al. 2020). Lu et al. (2021) also extracted the PJ pattern as an integral part of the most excitable global modes intrinsic to the summer climate system. The spatial structure of the PJ pattern depends on the configuration of local background mean flows, which is independent of external forcing. Nevertheless, the NWP background mean states change dramatically from early to mid- summer, then how will these changes lead to variations in the El Niño-excited circulation anomalies over the EA–NWP?

4.2 Variations in El Niño-excited PJ pattern from early to mid- summer(1)

Figures 5a–d show the composite vorticity anomalies at 850 hPa and 200 hPa and corresponding wave-activity fluxes in the early and mid- summer(1). Following Takaya and Nakamura (2001), the wave-activity fluxes are defined as:

$$W = \frac{1}{2|\overline{V}|}\begin{cases} \bar{u}(\psi_x'^2 - \psi'\psi_{xx}') + \bar{v}(\psi_x'\psi_y' - \psi'\psi_{xy}') \\ \bar{u}(\psi_x'\psi_y' - \psi'\psi_{xy}') + \bar{v}(\psi_y'^2 - \psi'\psi_{yy}') \\ f^2/S\left\{\bar{u}(\psi_x'\psi_p' - \psi'\psi_{xp}') + \bar{v}(\psi_y'\psi_p' - \psi'\psi_{yp}')\right\} \end{cases} \quad (1)$$

where $\vec{V}$ is the horizontal wind velocity vector, ψ the stream function, f the Coriolis parameter, $S = (R/p)(R\overline{T}/C_p p - d\overline{T}/dp)$ denotes the static stability, primes and overbars denote the composite atmospheric anomalies and climatological mean quantities, respectively. The direction of wave-activity fluxes denotes that of local group velocity of the stationary Rossby wave.

In both early and mid- summer(1), the vorticity anomalies mainly feature meridional wave structure from NWP to EA, corresponding to lower-level poleward wave-activity fluxes. However, the wave-activity fluxes between the two periods exhibit notable differences. The 850 hPa wave-activity fluxes in the mid-summer(1) are stronger and extend more northward than those in the early summer(1) (Figs. 5a, b). Notable upper-level equatorward wave-activity fluxes can be seen over the subtropical NWP in the mid-summer(1), while they are missing in the early summer(1) (Figs. 5c, d). The result suggests that the stationary Rossby wave activities associated with the AAC pattern are remarkably different between the two periods. Enhanced poleward propagation of stationary Rossby wave in the low troposphere and equatorward propagation in the upper troposphere indicate that the tropical–extratropical coupling over the EA–NWP is more robust in the mid-summer(1). As for its possible mechanism, Lu (2004) suggested that the easterly shear of background zonal mean flow over the NWP is robust in August while nearly neutral in June. This vertical shear plays an essential role in the emanation of heating-induced internal equatorial Rossby wave into the extratropics with a transformed barotropic structure (Wang and Xie 1996). Thus, the El Niño-excited NWP heating anomalies could induce more prominent circulation anomalies in mid–high latitudes of EA in the mid-summer(1) (Figs. 5a–d). Since the AAC is the lower-level tropical lobe of El Niño-excited PJ pattern, hereafter we focus on the El Niño-excited PJ pattern rather than the single AAC.

Figures 5e, f show the latitude–height function of 140°E composite vorticity anomalies in the early and mid- summer(1), respectively. In the early summer(1), the vorticity anomalies mainly feature a dipole structure, with phase tilting slight northward with height. The maximum negative and positive anomalies are distributed from 15°–20°N and 28°–33°N at lower troposphere, and are 25°–30°N and 35°–40°N at upper troposphere, highly resembling the PJ-related vorticity anomalies (Kosaka and Nakamura 2006). In the mid-summer(1), the vorticity anomalies at 140°E shift northward by about 5° relative to those in the early summer(1), with lower-level negative (positive) centers at ~20°N (38°N). Apart from the shift of locations, the northward tilting of vorticity anomalies with height in the mid-summer(1) is stronger than that in the early summer(1), suggesting an intensified atmospheric baroclinicity in the later period. On the coastal areas of EA, the temperature gradient between warm continent and cold ocean is beneficial for circulation anomalies tilting northward with height to gain available potential energy (*APE*) from the background mean flow (Kosaka and Nakamura 2006). The intensified upward wave-activity fluxes appear at high latitudes of EA in the mid-summer(1), implying that the El Niño-excited PJ pattern tends to extract *APE* from the background mean flow more efficiently in the mid-summer(1) than in the early summer(1). As a result, the three-dimensional meridional circulation system may develop stronger and last longer in the mid-summer(1).

Figures 5g, h show the longitude–height function of the composite vorticity anomalies at 40° and 48°N where the westerly jet cores in the early and mid- summer(1) are located (Figs. 4c–d), respectively. Significant positive vorticity anomalies tilt slightly westward with height from 130°–150°E in both early and mid- summer(1). Besides, there are pronounced upward wave-activity fluxes associated with the westward inclination in the mid-summer(1), suggesting an intensified upward propagation of wave energy in this period. Since the energy conversion efficiency depends on the relative position between background mean flow and the perturbations (Kosaka and Nakamura 2010), we further investigate the concrete energy conversion processes in the next sub-section.

4.3 Mechanisms for the intensification of El Niño-excited PJ pattern

4.3.1 Dry energy conversion

Following Kosaka and Nakamura (2010), the barotropic energy conversion (CK) from the background mean flow to perturbations can be given by

$$CK = \underbrace{\frac{(v'^2 - u'^2)}{2}\left(\frac{\partial \bar{u}}{\partial x} - \frac{\partial \bar{v}}{\partial y}\right)}_{CK_x} - \underbrace{u'v'\left(\frac{\partial \bar{u}}{\partial y} + \frac{\partial \bar{v}}{\partial x}\right)}_{CK_y} \quad (2)$$

where u and v denote the zonal and meridional winds, respectively. The baroclinic energy conversion (CP) from the background mean flow to perturbations is defined as

$$CP = \underbrace{\frac{Rf}{Sp}u'T'\frac{\partial \bar{v}}{\partial p}}_{CP_x} - \underbrace{\frac{Rf}{Sp}v'T'\frac{\partial \bar{u}}{\partial p}}_{CP_y} \quad (3)$$

where R denotes the gas constant, T the temperature, C_p the specific heat at constant pressure, and p the pressure. To objectively measure the efficiency of CK and CP in replenishing the El Niño-excited PJ pattern, we calculate dry energy conversion time scale: $\tau_{dry} = [KE + APE]/[CK + CP]$, where the bracket represents the area mean of 0–60°N, 110°–150°E. The major conclusions still hold even if the chosen area is slightly enlarged or shrank. Positive time scale less than 30 days indicates that the corresponding process is efficient enough to maintain the El Niño-excited PJ pattern, while positive time scale more than 30 days indicates the process is beneficial but not efficient. Negative time scale suggests that the process is detrimental to the maintenance of the El Niño-excited PJ pattern. More details about this framework could be found in Kosaka and Nakamura (2010). The τ_{dry} is 11.708 and 8.004 days in early and mid- summer(1), respectively (Table 1), suggesting the El Niño-excited PJ pattern can extract dry energy from the background mean flow more efficiently in the later period. As a result, the AAC intensifies in this period. We further investigate the relative role played by CK and CP in the following paragraphs.

Figure 6 shows the 850 hPa, 200 hPa and vertically integrated CK during early and mid- summer(1). At 850 hPa, pronounced positive CK lies on the climatological zonal winds' confluence zone ($\partial\bar{u}/\partial x < 0$) from the South China Sea to the east of the Philippine in both periods (Figs. 6a, b). The fixed position of positive CK by the NWP convergent background mean flow could explain, at least in part, why the southern flank of the AAC is anchored ~10°N in both early and mid- summer(1) (Fig. 2). Further analysis suggests that CK_x [especially -$(u'^2/2)(\partial\bar{u}/\partial x)$] plays a dominant role in inducing lower-level CK due to the zonally elongated shape of AAC ($u'^2 > v'^2$; figure not shown), emphasizing the importance of interaction between background zonal mean flow and circulation anomalies in triggering the AAC (Hu et al. 2019).

At 200 hPa, the positive and negative CK adjoin one another around the exit of the upper-level westerly jet ($\partial\bar{u}/\partial x < 0$). The westerly jet advances northward and weakens from early to mid- summer(1) and so does the CK along the westerly jet (Figs. 6c, d). Another conspicuous positive CK center is found in the Okhotsk sea in the mid-summer(1) (Fig. 6d). Since the directions of the wave-activity fluxes and momentum fluxes are opposite with each other, the salient equatorward wave-activity fluxes over the Okhotsk sea (Fig. 5d) denote strong poleward momentum fluxes ($u'v' > 0$). Thus, these poleward momentum fluxes to the north of the westerly jet core ($\partial\bar{u}/\partial y < 0$) favor the formation of positive CK [$-u'v'(\partial\bar{u}/\partial y) > 0$]. The positive centers in the vertically integrated CK reflect the characteristics of both the lower and upper levels (Figs. 6e, f).

The barotropic energy conversion time scale is defined as $\tau_{CK} = [KE]/[CK]$. The τ_{CK} is 10.687 and 13.206 days at 850 hPa, 13.117 and 107.152 days at 200 hPa, and 17.733 and 11.394 days when integrated vertically in the early and mid- summer(1), respectively (Table 1). The result indicates that CK is efficient in both early and mid-summer(1), but more efficient in the latter period. To put it in another way, the El Niño-excited PJ pattern can more efficiently gain barotropic energy from the background mean flow in the mid-summer(1) than in the early summer(1). It should also be noted that Eq. (1) dismisses the redistribution of KE from one area to the other, so the simple area average may import errors. However, this method is still a good way to quantify the wave–mean flow interactions preliminarily.

Figures 7a, b show the vertically integrated CP and climatological mean temperature at 500 hPa during early and mid- summer(1), respectively. The most pronounced positive CP over the EA in the early summer(1) is situated from the Bohai Sea to the Japan Sea. The positive CP advances northward to the Far East in the mid-summer(1), with its shape changing from the zonally-elongated to northeastward-slanted. We further decompose CP into CP_x and CP_y (Figs. 7c–f). CP_x makes marginal contributions in the early summer(1) but comes into play in the mid-summer(1). The positive CP_x over the Okhotsk sea in the mid-summer(1) facilitates the positive CP, resulting from an intensified interaction between eastward heat transport $(u'T' > 0)$ and thermal contrast between the warm continent and cold ocean $(\partial\bar{v}/\partial p > 0)$. Positive CP_y is of paramount importance in positive CP. Since the directions of the vertical wave fluxes and heat fluxes are the same, the salient upward wave fluxes denote strong poleward heat fluxes $(v'T' > 0)$. Due to the existence of meridional temperature gradient, $\partial\bar{u}/\partial p < 0$ exists in mid-latitudes of EA. Thus, the structure of westward tilt with height $(-v'T' < 0)$ is to the benefit of positive CP_y $(-v'T'(\partial\bar{u}/\partial p) > 0)$. The baroclinicity of the atmosphere is pronounced at mid–

high latitudes of EA, leading to stronger CP_y in the mid-summer(1). As a result, the El Niño-excited PJ pattern in the mid-summer(1) is more robust.

The efficiency of CP in replenishing the local APE of perturbations is measured by $\tau_{CP} = [APE]/[CP]$. The τ_{CP} is 7.067 and 4.513 days in early and mid- summer(1), respectively (Table 1), indicating that CP can energize the El Niño-excited PJ pattern more effectively in the mid-summer(1). Thus, CK and CP work together to intensify the El Niño-excited PJ pattern when the El Niño-induced SST forcing weakens in the mid-summer(1).

4.3.2 Moist feedback

It is worth noting that the PJ pattern is not only a dry dynamic mode that could sustain itself via dry energy conversion, but it could also interact with moist processes and be regarded as a moist dynamical mode (Kosaka and Nakamura 2010; Hirota and Takahashi 2012; Hu et al. 2019). Following Kosaka and Nakamura (2010), we attempt to quantify the moist processes in this sub-section and compare its efficiency with that of the dry energy conversion. The diabatic energy generation (CQ) can be written as

$$CQ = \frac{R^2}{Sp^2}\frac{T'Q'}{C_p} \tag{4}$$

where Q denotes the diabatic heating rate per unit mass (Yanai et al. 1973) and primes denote the composited anomalies. Q can be calculated from:

$$Q = C_p\left(\frac{\partial T}{\partial t} + \vec{V}\cdot\nabla T - \omega\sigma\right) \tag{5}$$

Here t denotes the time, ω the pressure velocity, and $\sigma = RT/C_p p - dT/dp$. Figure 8 shows the vertically integrated CQ during early and mid- summer(1). In the early summer(1), the positive CQ is situated in the subtropical NWP, which may be attributed to the El Niño-induced anomalous heating over the NWP (Xie et al. 2009; Xiang et al. 2013). The positive CQ over the NWP intensifies in the mid-summer(1) due to the onset of the climatological NWP summer monsoon.

We measure the efficiency of CQ in replenishing the total energy of perturbations via $\tau_{moist} = [KE + APE]/[CQ]$. The τ_{moist} is 20.635 and 3.879 days in early and mid- summer(1), respectively (Table 1). It suggests that CQ will energize the El Niño-excited PJ pattern more efficiently in the mid-summer(1). Since the climatological mean precipitation over the NWP enhances from early to mid- summer, the local atmospheric response becomes more sensitive to external forcings like El Niño-induced SST anomalies (Xie et al. 2009; Wu et al. 2010), thus an intensified El Niño-excited PJ pattern will ensue.

Here, we conclude that both the dry energy conversion and moist feedback are of vital importance in the intensification of the El Niño-excited PJ pattern. And the comparison of efficiency between dry processes and moist process (Table 1) indicates that the diabatic energy generation may be more efficient than dry (barotropic and baroclinic) energy conversion in maintaining the El Niño-excited PJ pattern in the mid-summer(1), while less efficient in the early summer(1). We further measure the efficiency of CK, CP and CQ in replenishing the total energy via $\tau_{total} = [KE + APE]/[CK + CP + CQ]$. The τ_{total} is 7.469 and 2.613 days in early and mid-summer(1), respectively (Table 1). It suggests the efficiency of energy conversions/generation between the local mean state and the El Niño-excited PJ pattern is higher in the mid-summer(1), hence the El Niño-excited PJ pattern is prone to be stronger.

4.4 Mechanisms for the northward extension of El Niño-excited PJ pattern

In the last sub-section, we investigate the mechanisms for the intensification of the El Niño-excited PJ pattern in the mid-summer(1) via comparison of energy conversion/generation efficiencies in the two periods. In this sub-section, we further discuss the mechanisms for the northward extension of El Niño-excited PJ pattern. Kosaka and Nakamura (2010) demonstrated that the mode which can extract energy from background mean flows most efficiently is the one most sustainable. Thus, every mode has a preferred latitude or longitude phase. Here, we analyze whether the El Niño-excited PJ patterns in the early and mid- summer(1) are the dynamic modes inherent in the background mean flows, which can maximize the efficiency of dry energy conversion.

Following Kosaka and Nakamura (2010), we artificially displace the El Niño-excited PJ pattern by every 5° in latitude, while the climatological background mean flows are fixed. Table 2 gives the time scales with which the El Niño-excited PJ pattern could gain energy after the anomalous circulation pattern is shifted meridionally relative to its original location. The result shows that the El Niño-excited PJ patterns in both two periods gain dry energy from background mean flows most efficiently at the original latitude. That is to say, the El Niño-excited PJ patterns in the early and mid-summer(1) are both the dynamic modes and their locations are fixed meridionally according to the configuration of local background mean flows. As the background mean flows shift northward from the early to mid- summer(1) (Fig. 4), the dynamic mode also extends northward.

It should also be noted that the artificially displaced circulation anomalies no longer meet the thermal or vorticity balance, so we verify the results by additional empirical orthogonal function (EOF) analyses. We perform EOF analyses on the 850 hPa vorticity anomalies over the EA–NWP (10°–60°N, 100°–160°E) from 1979 to 2016 in the early and mid- summer, respectively (Figs. 9a, b). The domain of EOF analysis is same as that in Kubota et al. (2016). The leading EOF modes in the early and mid- summer explain 18.094% and 20.21%, respectively, both are well separated with other modes by the criterion of North et al. (1982). The EOF1 modes feature an AAC pattern over the NWP in early and mid- summer, while extending more northward in the later period. Since the EOF1 normally captures the dominant mode of the interannual variability, the result suggests that the circulation anomalies over the EA–NWP tend to occur in a more northward position in the mid-summer. PC1s in the early and mid- summer are highly correlated with DJF(0) Niño3.4 index ($r = 0.46$ and 0.466, respectively, both $p < 0.01$, $n = 38$).

We further use partial correlation method to remove the influence of ENSO, and perform EOF analyses again on the residues in the early and mid- summer(1), respectively (Figs. 9c, d). Thus, we get the dominant mode of atmospheric interannual variability over the EA–NWP independent of ENSO. The patterns are quite similar with those in the original field, and the differences between them are mainly in the explained variance. The result further confirms that the observed northward extension of El Niño-excited PJ pattern in the mid-summer(1) stems from the northward extension of the local internal dynamic mode in the mid-summer (not only occurs in several El Niño decaying years, but in every year), whose spatial pattern depends on the configuration of local mean flows instead of external forcings like ENSO.

5. Conclusions and discussion

5.1 Conclusions

In the present study, we investigate the intra-seasonal variations of the AAC during El Niño decaying summer and explain these phenomena from the perspective of energetics. The AAC is stronger and more northward-extended in July(1) and August(1) than in June(1), while the decaying SST anomalies over the NIO, NA and NWP could not account for this shift (Fig. 1), leading people to look for other factors besides the El Niño-induced SST anomalies. Based on daily datasets, we further divide the study period into early summer (15 June–14 July) and mid-summer (20 July–18 August), which is more accurate than month division since the most pronounced AAC transition occurs in late July(1) (Fig. 2). Through the intra-seasonal variations of the AAC, the decaying El Niño could strengthen the climatological northward migration and intensification of WPSH over the North Pacific while hinder the climatological northward migration of WPSH over eastern China (Fig. 3).

Then we diagnose the variations of El Niño-excited PJ pattern based on the theoretical framework developed by Kosaka and Nakamura (2010) and draw the following three major conclusions as shown in Fig. 10. Since the present study suggests that the intra-seasonal variations of AAC are induced by local mean state changes, the following conclusions could also be applied in La Niña decaying summer.

First, El Niño will excite more prominent circulation anomalies at high latitudes of EA in the mid-summer(1) than in the early summer(1), associated with more salient lower-level poleward wave-activity fluxes originating from the subtropical NWP and injecting upward in the upstream of westerly jet exit in the mid-summer(1) (Fig. 5). The result suggests that the tropical–extratropical coupling over the EA–NWP is more robust in the mid-summer(1) from the view of atmospheric wave. Thus, the extratropical circulation of EA may be of a higher predictability in the mid-summer(1). Lu (2004) suggested that the easterly shear of background zonal mean flow over the NWP is robust in August while nearly neutral in June, therefore the El Niño-induced baroclinic disturbances over the NWP could be transformed into a barotropic structure in the mid-summer(1) but not in the early summer(1). Since only the barotropic structure of disturbances could be conveyed to the extratropics (Wang and Xie 1996), the El Niño-excited NWP heating anomalies could induce more prominent circulation anomalies in mid–high latitudes of EA in the mid-summer(1).

Second, dry energy conversion from the background mean flow to perturbations over the EA–NWP is more efficient in the mid-summer(1) than in the early summer(1), well explaining the intensification of El Niño-excited PJ pattern (Table 1). CK and CP (especially CP_y) both play an important role in this process (Figs. 6, 7). The moist feedback of the El Niño-excited PJ pattern is also enhanced in the mid-summer(1) (Fig. 8) due to the onset of the climatological NWP summer monsoon (Figs. 4a, b), contributing to the intensification of El Niño-excited PJ pattern. The comparison of efficiency between dry processes and moist process indicates that the diabatic energy generation may be more efficient than dry (barotropic plus baroclinic) energy conversions in maintaining the El Niño-excited PJ pattern in the mid-summer(1), while less efficient in the early summer(1). Although the El Niño-induced SST anomalies decay in the mid-summer(1), the NWP atmospheric internal dynamics modulated by local mean states strengthen in this period, leading to the intensified AAC. Our findings highlight that both the El Niño-induced SST anomalies and local atmospheric internal dynamics are important for the evolution of AAC in El Niño decaying summer, while the role of the latter is often underestimated in the previous studies.

Third, through artificially displacing the El Niño-excited PJ pattern in the meridional direction, it is found that only at the original latitude can the El Niño-excited PJ pattern gain dry energy from the background mean flows most efficiently (Table 2), suggesting that the original latitude is the preferred latitude of the El Niño-excited PJ pattern. Mean state changes over the EA–NWP from early to mid- summer favor the northward shift of the preferred latitude of the circulation anomalies. Thus, the El Niño-excited PJ pattern is more northward-extended in the mid-summer(1). Additional EOF analyses further confirm that the northward extension of El Niño-excited PJ pattern stems from changes of local internal dynamic mode from early to mid- summer (Fig. 9), which is independent of external forcings like ENSO.

5.2 Discussion

In the present study, we calculate the efficiencies of energy conversion/generation to explain the intensification of the AAC. Moreover, we use perturbation displacement method and EOF to discover the internal dynamic mode over the EA–NWP and further explain the northward extension of the AAC. In fact, the above two points of view are not independent but complementary to each other. The northward shift of *CK, CP* and *CQ* in the mid-summer(1) (Figs. 6, 7, 8) can also explain the northward extension of the AAC while the enhanced internal dynamic mode in the mid-summer (Figs. 9a, b) can also elucidate the intensification of the AAC. Since every method has its limitation, this cross-validation thought is frequently used in the energetics to increase the reliability of the conclusion (Kosaka and Nakamura 2010).

Besides, although the results shown in the present study are confined to the AAC during El Niño decaying summer, local mean state changes may induce intensification and northward extension of all intra-seasonal and monthly perturbations over the EA–NWP in the mid-summer, expanding the implications of the present study. The pioneering work by Tsuyuki and Kurihara (1989) suggested that the intra-seasonal PJ pattern is inclined to be more significant in the mid-summer than in the early summer, supporting this hypothesis. On the other hand, this study only focuses on the period from 1979 to 2016. Some evidences (Ye and Lu 2010; Yang and Huang 2021) show that the impact of ENSO varies on multidecadal timescale, and is likely modulated by the global warming (Hu et al. 2021). Whether the intra-seasonal variations of the AAC pattern in El Niño decaying summer vary on multidecadal timescale deserves further study.

Acknowledgements: The work was supported by the National Key R&D Program of China (Fund No: 2019YFA0606703), the Second Tibetan Plateau Scientific Expedition and Research (STEP) program (grant no. 2019QZKK0102), the Strategic Priority Research Program of Chinese Academy of Sciences (XDA20060500), National Natural Science Foundation of China (41775086, 41831175), Key Deployment Project of Centre for Ocean Mega-Research of Science, Chinese Academy of Sciences (COMS2019Q03), and the Youth Innovation Promotion Association of CAS.

References

Alexander MA, Bladé I, Newman M, Lanzante JR, Lau NC, Scott JD (2002) 2002: The atmospheric bridge: The influence of ENSO teleconnections on air–sea interaction over the global oceans. J Climate 15 (16):2205–2231

Branstator G (1985) Analysis of General Circulation Model Sea-Surface Temperature Anomaly Simulations Using a Linear Model. Part I: Forced Solutions. J Atmos Sci 42 (21):2225–2241

Chang CP, Zhang Y, Li T (2000) Interannual and Interdecadal Variations of the East Asian Summer Monsoon and Tropical Pacific SSTs. Part I: Roles of the Subtropical Ridge. J Clim 13 (24):4310–4325

Du Y, Xie S-P, Huang G, Hu K (2009) Role of Air–Sea Interaction in the Long Persistence of El Niño–Induced North Indian Ocean Warming. J Clim 22 (8):2023–2038

Du Y, Yang L, Xie SP (2011) Tropical Indian Ocean Influence on Northwest Pacific Tropical Cyclones in Summer Following Strong El NinoEl Niño. J Clim 24 (1):315–322

Fu C, Ye D (1988) The Tropical Very Low-Frequency Oscillation on Interannual Scale. Adv Atmos Sci 5 (3):369–388

Hirota N, Takahashi M (2012) A tripolar pattern as an internal mode of the East Asian summer monsoon. Clim Dyn 39:2219–2238

Hu K, Huang G, Huang R (2011) The Impact of Tropical Indian Ocean Variability on Summer Surface Air Temperature in China. J Clim 24 (20):5365–5377

Hu K, Huang G, Qu X, Huang R (2012) The impact of Indian Ocean variability on high temperature extremes across the southern Yangtze River valley in late summer. Adv Atmos Sci 29 (1):91–100

Hu K, Huang G, Xie S-P, Long S-M (2019) Effect of the mean flow on the anomalous anticyclone over the Indo-Northwest Pacific in post-El Niño summers. Clim Dyn 53 (9-10):5725–5741

Hu K, Xie S-P, Huang G (2017) Orographically Anchored El Niño Effect on Summer Rainfall in Central China. J Clim 30 (24):10037–10045

Hu K, Huang G, Huang P, Kosaka Y, Xie S-P (2021) Intensification of El Niño-induced atmospheric anomalies under greenhouse warming. Nature Geoscience. (in press)

Huang B, Kinter JL III (2002) Interannual variability in the tropical Indian Ocean. J Geophys Res 107(C11):3199

Huang R, Chen J, Huang G (2007) Characteristics and Variations of the East Asian Monsoon System and Its Impacts on Climate Disasters in China. Adv Atmos Sci 24:993–1023

Huang R, Wu Y (1989) The Influence of ENSO on the Summer Climate Change in China and Its Mechanism. Adv Atmos Sci 6 (1):21–32

Kanamitsu M, Ebisuzaki W, Woollen J, Yang SK, Hnilo JJ, Fiorino M, Potter GL (2002) NCEP–DOE AMIP-II Reanalysis (R-2). Bull Am Meteorol Soc 83 (11):1631–1643

Kim S, Kug J-S (2021) Delayed Impact of Indian Ocean Warming on the East Asian Surface Temperature Variation in Boreal Summer. J Clim 34 (8):3255–3270

Klein SA, Soden BJ, Lau NC (1999) Remote Sea Surface Temperature Variations during ENSO: Evidence for a Tropical Atmospheric Bridge. J Clim 12 (4):917–932

Kong W, Chiang JCH (2020) Southward Shift of Westerlies Intensifies the East Asian Early Summer Rainband Following El Niño. Geophys Res Lett 47 (17)

Kosaka Y, Nakamura H (2006) Structure and dynamics of the summertime Pacific–Japan teleconnection pattern. Q J R Meteorol Soc 132 (619):2009–2030

Kosaka Y, Nakamura H (2010) Mechanisms of Meridional Teleconnection Observed between a Summer Monsoon System and a Subtropical Anticyclone. Part I: The Pacific–Japan Pattern. J Clim 23 (19):5085–5108

Kosaka Y, Xie SP, Lau NC, Vecchi GA (2013) Origin of seasonal predictability for summer climate over the Northwestern Pacific. Proc Natl Acad Sci 110 (19):7574–7579

Kubota H, Kosaka Y, Xie S-P (2016) A 117-year long index of the Pacific-Japan pattern with application to interdecadal variability. Int J Climatol 36 (4):1575–1589

Li X, Lu R (2018) Subseasonal Change in the Seesaw Pattern of Precipitation between the Yangtze River Basin and the Tropical Western North Pacific during Summer. Adv Atmos Sci 35 (10):1231–1242

Li T, Wang B, Wu B, Zhou T, Chang CP, Zhang R (2017) Theories on formation of an anomalous anticyclone in western North Pacific during El Niño: A review. J Meteor Res 31:987–1006

Liebmann B, Smith CA (1996) Description of a Complete (Interpolated) Outgoing Longwave Radiation Dataset. Bull Am Meteorol Soc 77:1275–1277

Lin Z, Lu R (2008) Abrupt Northward Jump of the East Asian Upper-Tropospheric Jet Stream in Mid-Summer. J Meteorol Soci Jpn 86 (6):857–866

Lu J, Xue D, Leung LR, Liu F, Song F, Harrop B, Zhou W (2021) The Leading Modes of Asian Summer Monsoon Variability as Pulses of Atmospheric Energy Flow. Geophys Res Lett 48 (5):e2020GL091629

Lu R (2004) Associations among the Components of the East Asian Summer Monsoon System in the Meridional Direction. J Meteorol Soci Jpn 82 (1):155–165

Lu R, Lin Z (2009) Role of Subtropical Precipitation Anomalies in Maintaining the Summertime Meridional Teleconnection over the Western North Pacific and East Asia. J Clim 22 (8):2058–2072

Lu R, Lu S (2014) Local and remote factors affecting the SST–precipitation relationship over the western North Pacific during summer. J Clim 27:5132–5147

Nitta T (1987) Convective activities in the tropical western Pacific and their impact on the northern hemisphere summer circulation. J Meteorol Soci Jpn 65:165–171

North GR, Bell TL, Cahalan RF, Moeng FJ (1982) Sampling errors in the estimation of empirical orthogonal functions. Mon Weather Rev 110 (7):699–706

Rayner N, Parker D, Horton E, Folland C, Alexander L, Rowell D, Kent E, Kaplan A (2003) Global analyses of sea surface temperature, sea ice, and night marine air temperature since the late nineteenth century. J Geophys Res Atmos 108 (D14):4407

Rong X, Zhang R, Li T (2010) Impacts of Atlantic sea surface temperature anomalies on Indo-East Asian summer monsoon-ENSO relationship. Chin Sci Bull 55 (22):2458–2468

Simmons A, Wallace J, Branstator G (1983) Barotropic wave propagation and instability, and atmospheric teleconnection patterns. J Atmos Sci 40:1363–1392

Takaya K, Nakamura H (2001) A Formulation of a Phase-Independent Wave-Activity Flux for Stationary and Migratory Quasigeostrophic Eddies on a Zonally Varying Basic Flow. J Atmos Sci 58 (6):608–627

Tao SY, Chen LX (1987) A review of recent research on the East Asian summer monsoon in China. Monsoon meteorology (Chang CP, Krishnamurti TN (eds)). Oxford University Press, New York

Tsuyuki T, Kurihara K (1989) Impact of Convective Activity in the Western Tropical Pacific on the East Asian Summer Circulation. J Meteorol Soci Jpn 67 (2):231–247

Wang B, Xie X (1996) Low-Frequency Equatorial Waves in Vertically Sheared Zonal Flow. Part I: Stable Waves. J Atmos Sci 53 (23):449–467

Wang B, Wu R, Fu X (2000) Pacific-East Asian Teleconnection: How Does ENSO Affect East Asian Climate? J Clim 13 (9):1517–1536

Wang B, Wu R, Lau KM (2001) Interannual Variability of the Asian Summer Monsoon: Contrasts between the Indian and the Western North Pacific–East Asian Monsoons. J Clim 14 (20):4073–4090

Wang B, Wu R, Li T (2003) Atmosphere–Warm Ocean Interaction and Its Impacts on Asian–Australian Monsoon Variation. J Clim 16 (8):1195–1211

Wang C-Y, Xie S-P, Kosaka Y (2018) Indo-Western Pacific Climate Variability: ENSO Forcing and Internal Dynamics in a Tropical Pacific Pacemaker Simulation. J Clim 31 (24):10123–10139

Wang X, Xie S-P, Guan Z (2020) Atmospheric Internal Variability in the Summer Indo–Northwestern Pacific: Role of the Intra-seasonal Oscillation. J Clim 33 (8):3395–3410

Wang X, Xie S-P, Guan Z, Wang M (2021) A Common Base Mode of Asian Summer Monsoon Variability across Timescales. J Clim 1–38.

Wei, K., C. Ouyang, H. Duan, Y. Li, M. Chen, J. Ma, H. An and S. Zhou (2020) Reflections on the catastrophic 2020 yangtze river basin flooding in southern china. The Innovation 2(1):100038

Wu B, Li T, Zhou T (2010) Relative Contributions of the Indian Ocean and Local SST Anomalies to the Maintenance of the Western North Pacific Anomalous Anticyclone during the El Niño Decaying Summer. J Clim 23 (11):2974–2986

Xiang B, Wang B, Yu W, Xu S (2013) How can anomalous western North Pacific Subtropical High intensify in late summer? Geophys Res Lett 40 (10):2349–2354

Xie P, Arkin PA (1997) Global precipitaion: A 17-year monthly analysis based on gauge observations, satellite estimates. Bull Am Meteorol Soc 78 (11):2539–2558

Xie S-P, Hu K, Hafner J, Tokinaga H, Du Y, Huang G, Sampe T (2009) Indian Ocean Capacitor Effect on Indo–Western Pacific Climate during the Summer following El Niño. J Clim 22 (3):730–747

Xie S-P, Kosaka Y, Du Y, Hu K, Chowdary JS, Huang G (2016) Indo-western Pacific ocean capacitor and coherent climate anomalies in post-ENSO summer: A review. Adv Atmos Sci 33 (4):411–432

Xie SP, Annamalai H, Schott FA, Mccreary JP (2002) Structure and Mechanisms of South Indian Ocean Climate Variability. J Clim 15 (8):864–878

Xu P, Wang L, Chen W, Feng J, Liu Y (2019) Structural Changes in the Pacific–Japan Pattern in the Late 1990s. J Clim 32 (2):607–621

Yanai M, Esbensen S, Chu J-H (1973) Determination of bulk properties of tropical cloud clusters from large-scale heat and moisture budgets. J Atmos Sci 30(4):611–627

Yang X, Huang P (2021) Restored relationship between ENSO and Indian summer monsoon rainfall around 1999/2000. The Innovation 2 (2):100102.

Ye H, Lu R (2010) Subseasonal Variation in ENSO-Related East Asian Rainfall Anomalies during Summer and Its Role in Weakening the Relationship between the ENSO and Summer Rainfall in Eastern China since the Late 1970s. J Clim 24 (9):2271–2284

Zhang R, Sumi A, Kimoto M (1996) Impact of El Niño on the East Asian monsoon : A diagnostic study of the '86/87 and '91/92 events. J Meteorol Soci Jpn 74 (1):49–62

Zhou W, Xie S-P, Zhou Z-Q (2016) Slow Preconditioning for the Abrupt Convective Jump over the Northwest Pacific during Summer. J Clim 29 (22):8103–8113

Zhou Z-Q, Xie S-P, Zhang G, Zhou W (2018) Evaluating AMIP Skill in Simulating Interannual Variability over the Indo-Western Pacific. J Clim 31 (6):2253–2265

Zhu Y, Wen Z, Guo Y, Chen R, Li X, Qiao Y (2020) The characteristics and possible growth mechanisms of the quasi-biweekly Pacific–Japan teleconnection in Boreal Summer. Clim Dyn 55:3363–3380

Figure Captions:

Figure 1. (Left) 850 hPa wind (m/s, vectors) and SAT (K, colors) anomalies, (middle) vertically integrated (from the surface to 200 hPa) moisture fluxes (kg/m/s, vectors) and their divergence (mm/day, colors), (right) SST anomalies (K, colors) in (a, b, c) June, (d, e, f) July, (g, h, i) August for the El Niño composite. Vectors only exceeding the 90% confidence level are shown and dots indicate that the anomalies are significant at the 90% confidence level. The hatched areas from west to east in (c) indicate NA, NIO and subtropical NWP, respectively.

Figure 2. 850 hPa wind (m/s, vectors, shown only exceeding the 90% confidence level), precipitation (mm/day, colors, dots indicate that the anomalies are significant at the 90% confidence level) and OLR (W/m^2, contours for ±5, ±10, ±15, ±20) anomalies averaged between 110°–150°E for the El Niño composite. Solid and dashed contours represent negative and positive convection anomalies, respectively. Early summer is defined as 15 June–14 July and mid-summer 20 July–18 August.

Figure 3. Climatological mean 500 hPa winds (m/s, vectors) and SLP (hPa, colors) in the early summer (a), mid-summer (b) and their differences (c). Anomalous 500 hPa winds (m/s, vectors, shown only exceeding the 90% confidence level) and SLP (hPa, colors, dots indicate that the anomalies are significant at the 90% confidence level) for the El Niño composite during El Niño decaying early summer (d), mid-summer (e) and their differences (f).

Figure 4. Climatological mean horizonal winds (m/s, vectors) at 850 hPa (a, b) and 200 hPa (c, d), superimposed on the climatological mean precipitation (mm/day, colors; a, b) and air temperature at 500 hPa (°C, colors; c, d) in the early and mid- summer. Climatological mean zonal winds are also overlaid (m/s, contours for 15, 20, 25, 30; c, d).

Figure 5. Relative vorticity anomalies (colors, dots indicate that the anomalies are significant at the 90% confidence level) at (a, b) 850 hPa and (c, d) 200 hPa in (a, c) early summer, (b, d) mid-summer for the El Niño composite. Meridional section of composite vorticity anomalies (colors) at (e, f) 140°E in the early and mid- summer(1), respectively. Zonal section of composite vorticity anomalies (colors) at (g) 40° and (h) 48°N in the early and mid- summer(1), respectively. Vectors denote the corresponding wave-activity fluxes.

Figure 6. 850 hPa, 200 hPa and vertically integrated (1000–200 hPa) barotropic energy conversion CK during El Niño decaying early summer (a, c, e) and mid-summer (b, d, f).

Figure 7. Vertically integrated (1000–200 hPa) baroclinic energy conversion CP ($\times\ 10^{-3} Kg \cdot m^2 \cdot s^{-3}$, colors) and climatological mean temperature at 500 hPa (°C, contours for -16, -14, -12, -10, -8, -6, -4, -2) during El Niño decaying early summer (a) and mid-summer (b). Also

shown are CP_x and CP_y in the Eq. (2) during El Niño decaying early summer (c, e) and mid-summer (d, f).

Figure 8. Vertically integrated (1000–200 hPa) diabatic energy generation CQ ($\times 10^{-2} W \cdot m^{-2}$, colors) during El Niño decaying early summer (a) and mid-summer (b).

Figure 9. 850 hPa wind anomalies (vectors) regressed against standardized PC1 of the EOF analyses performed on standardized 850 hPa vorticity anomalies over the EA–NWP (10°–60°N, 100°–160°E) during El Niño decaying early summer (a) and mid-summer (b). c (d) is the same as a (b) but on the 850 hPa vorticity anomalies independent of ENSO. Vectors only exceeding the 90% confidence level are shown.

Figure 10. Schematic diagram illustrating the intra-seasonal variations of ENSO-excited PJ pattern during ENSO decaying summer.

Table 1. Time scales (days) with which the El Niño-excited PJ pattern could gain energy (KE for τ_{CK}, APE for τ_{CP}, and $KE + APE$ for τ_{dry}, τ_{moist}, and τ_{total}) through energy conversions (CK for τ_{CK}, CP for τ_{CP}, and $CK + CP$ for τ_{dry}), diabatic energy generation (CQ for τ_{moist}) and their sum ($CK + CP + CQ$ for τ_{total}) during El Niño decaying early and mid-summer. The eddy energy and energy conversions/generation are integrated vertically from 1000 to 200 hPa and then horizontally over 0–60°N, 110°–150°E.

0–60°N, 110°–150°E		Early summer(1)	Mid-summer(1)
	850 hPa/ lower level	10.687	13.206
τ_{CK}	200 hPa/ upper level	13.117	107.152
	Vertical integral	17.733	11.394
τ_{CP}	Vertical integral	7.067	4.513
τ_{dry}	Vertical integral	11.708	8.004
τ_{moist}	Vertical integral	20.635	3.879
τ_{total}	Vertical integral	7.469	2.613

Table 2. Time scales (days) with which the El Niño-excited PJ pattern could gain energy after the anomalous circulation pattern is shifted meridionally relative to its original location. The eddy energy is calculated from the original anomalous circulation pattern and integrated over 0–60°N, 110°–150°E, whereas the energy conversions are integrated over the new domain shifted with the anomalous circulation pattern. Both the eddy energy and energy conversions are integrated vertically from 1000 to 200 hPa before integrated horizontally. The efficiencies at the original latitude are highlighted in shadow.

	τ_{CK}		τ_{CP}		τ_{dry}	
	Early summer(1)	Mid-summer(1)	Early summer(1)	Mid-summer(1)	Early summer(1)	Mid-summer(1)
15° northward	-22.529	-32.861	6.506	5.287	43.173	32.739
10° northward	-21.538	252.399	7.779	4.245	75.529	14.648
5° northward	68.603	17.472	6.444	4.271	15.994	9.402
Original	17.733	11.394	7.067	4.513	11.708	8.004
5° southward	24.152	20.841	13.767	5.471	19.211	11.707
10° southward	17.405	-46.151	34.212	6.516	20.907	37.085
15° southward	8.859	-19.514	-13.347	6.142	20.477	121.957

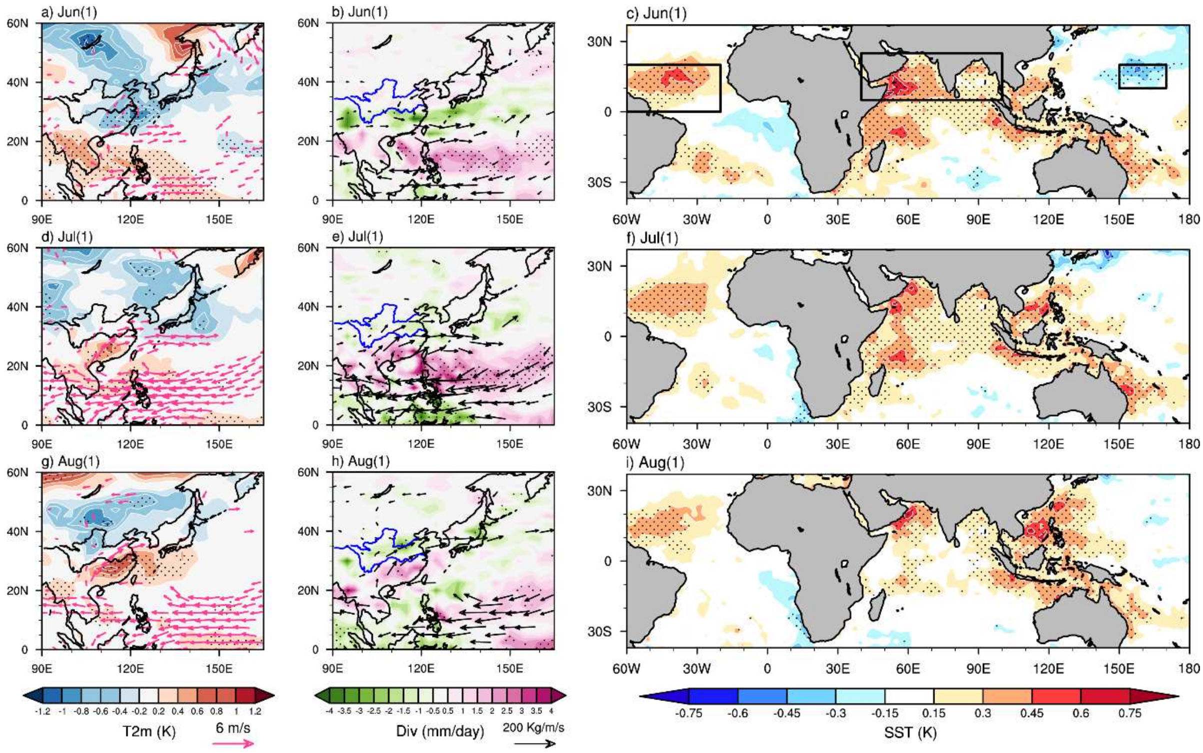

Figure 1. (Left) 850 hPa wind (m/s, vectors) and SAT (K, colors) anomalies, (middle) vertically integrated (from the surface to 200 hPa) moisture fluxes (kg/m/s, vectors) and their divergence (mm/day, colors), (right) SST anomalies (K, colors) in (a, b, c) June, (d, e, f) July, (g, h, i) August for the El Niño composite. Vectors only exceeding the 90% confidence level are shown and dots indicate that the anomalies are significant at the 90% confidence level. The hatched areas from west to east in (c) indicate NA, NIO and subtropical NWP, respectively.

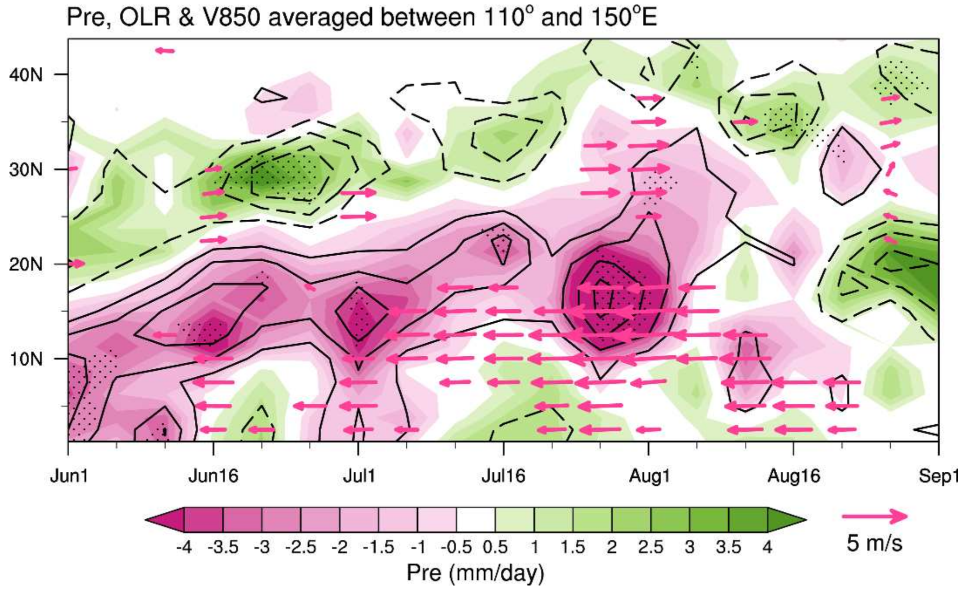

Figure 2. 850 hPa wind (m/s, vectors, shown only exceeding the 90% confidence level), precipitation (mm/day, colors, dots indicate that the anomalies are significant at the 90% confidence level) and OLR (W/m^2, contours for ±5, ±10, ±15, ±20) anomalies averaged between 110°–150°E for the El Niño composite. Solid and dashed contours represent negative and positive convection anomalies, respectively. Early summer is defined as 15 June–14 July and mid-summer 20 July–18 August.

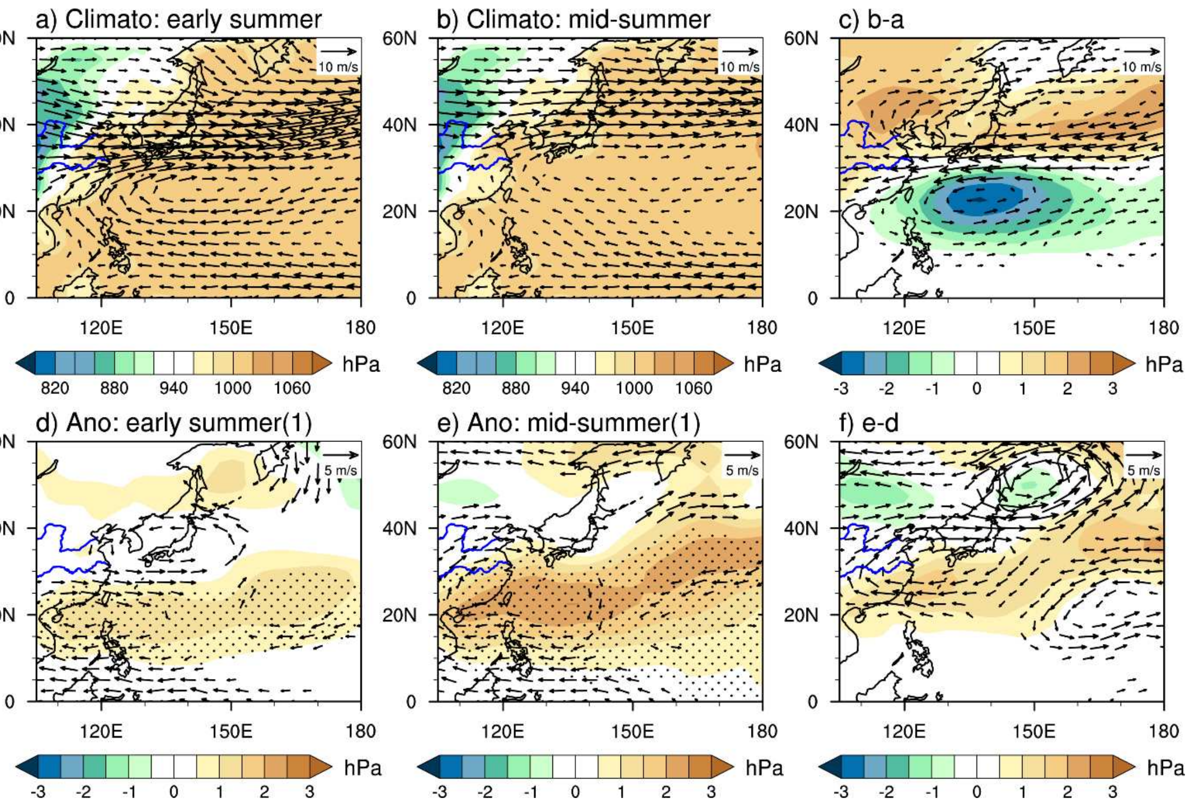

Figure 3. Climatological mean 500 hPa winds (m/s, vectors) and SLP (hPa, colors) in the early summer (a), mid-summer (b) and their differences (c). Anomalous 500 hPa winds (m/s, vectors, shown only exceeding the 90% confidence level) and SLP (hPa, colors, dots indicate that the anomalies are significant at the 90% confidence level) for the El Niño composite during El Niño decaying early summer (d), mid-summer (e) and their differences (f).

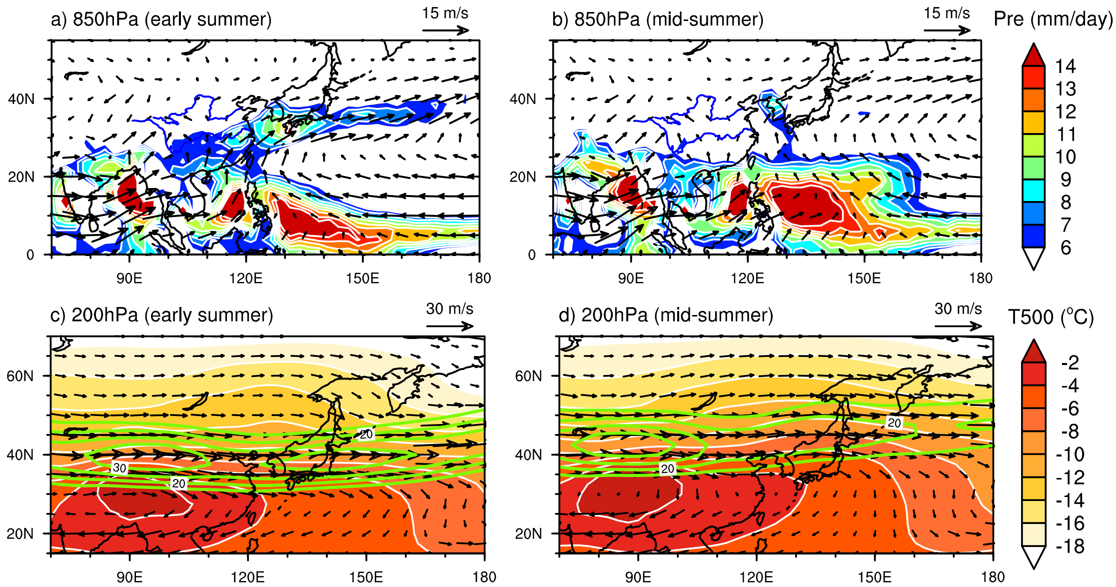

Figure 4. Climatological mean horizontal winds (m/s, vectors) at 850 hPa (a, b) and 200 hPa (c, d), superimposed on the climatological mean precipitation (mm/day, colors; a, b) and air temperature at 500 hPa (°C, colors; c, d) in the early and mid- summer. Climatological mean zonal winds are also overlaid (m/s, contours for 15, 20, 25, 30; c, d).

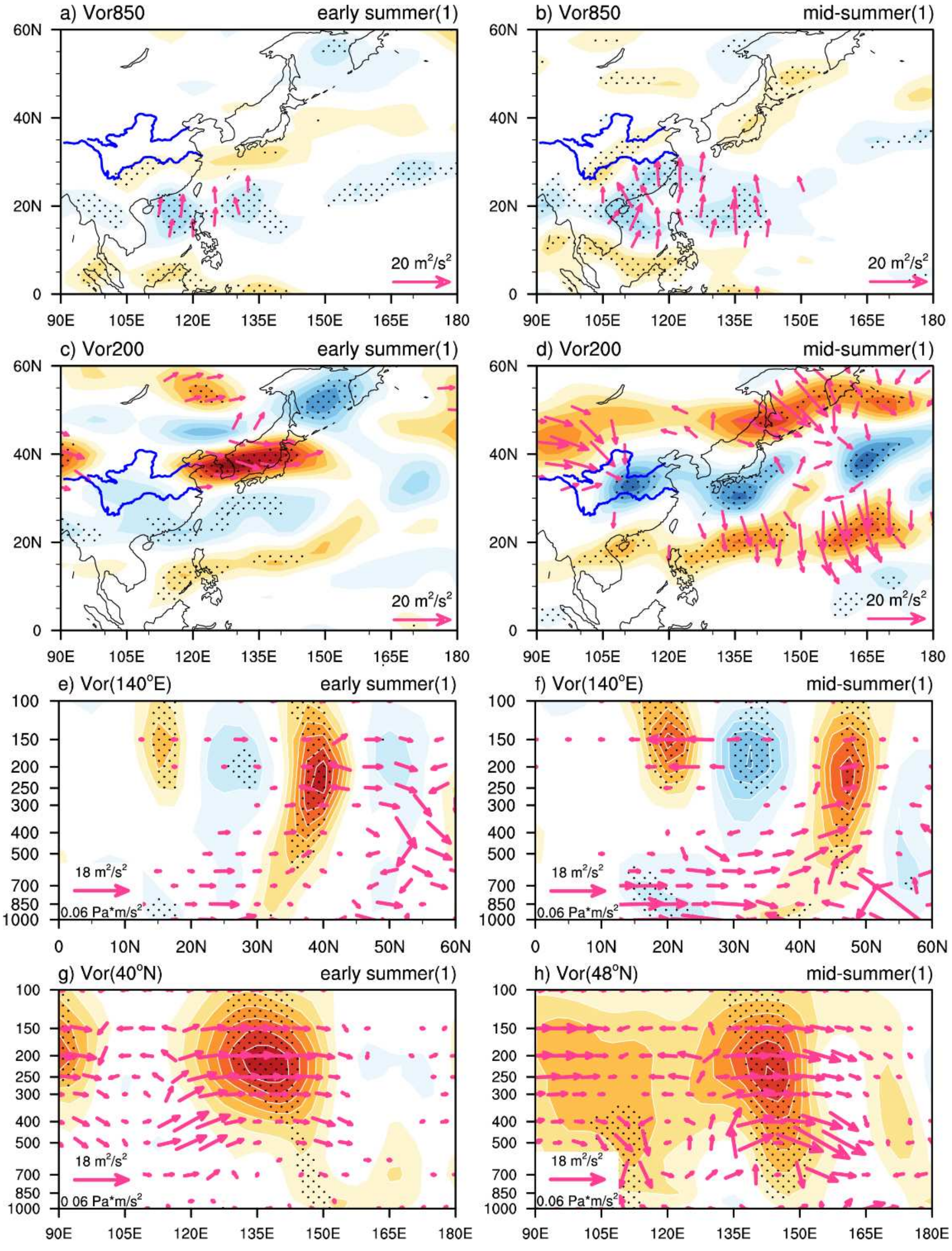

Figure 5. Relative vorticity anomalies ($\times 10^{-6}s^{-1}$, colors, dots indicate that the anomalies are significant at the 90% confidence level) at (a, b) 850 hPa and (c, d) 200 hPa in (a, c) early summer, (b, d) mid-summer for the El Niño composite. Meridional section of composite vorticity anomalies (colors) at (e, f) 140°E in the early and mid- summer(1), respectively. Zonal section of composite vorticity anomalies (colors) at (g) 40° and (h) 48°N in the early and mid-summer(1), respectively. Vectors denote the corresponding wave-activity fluxes.

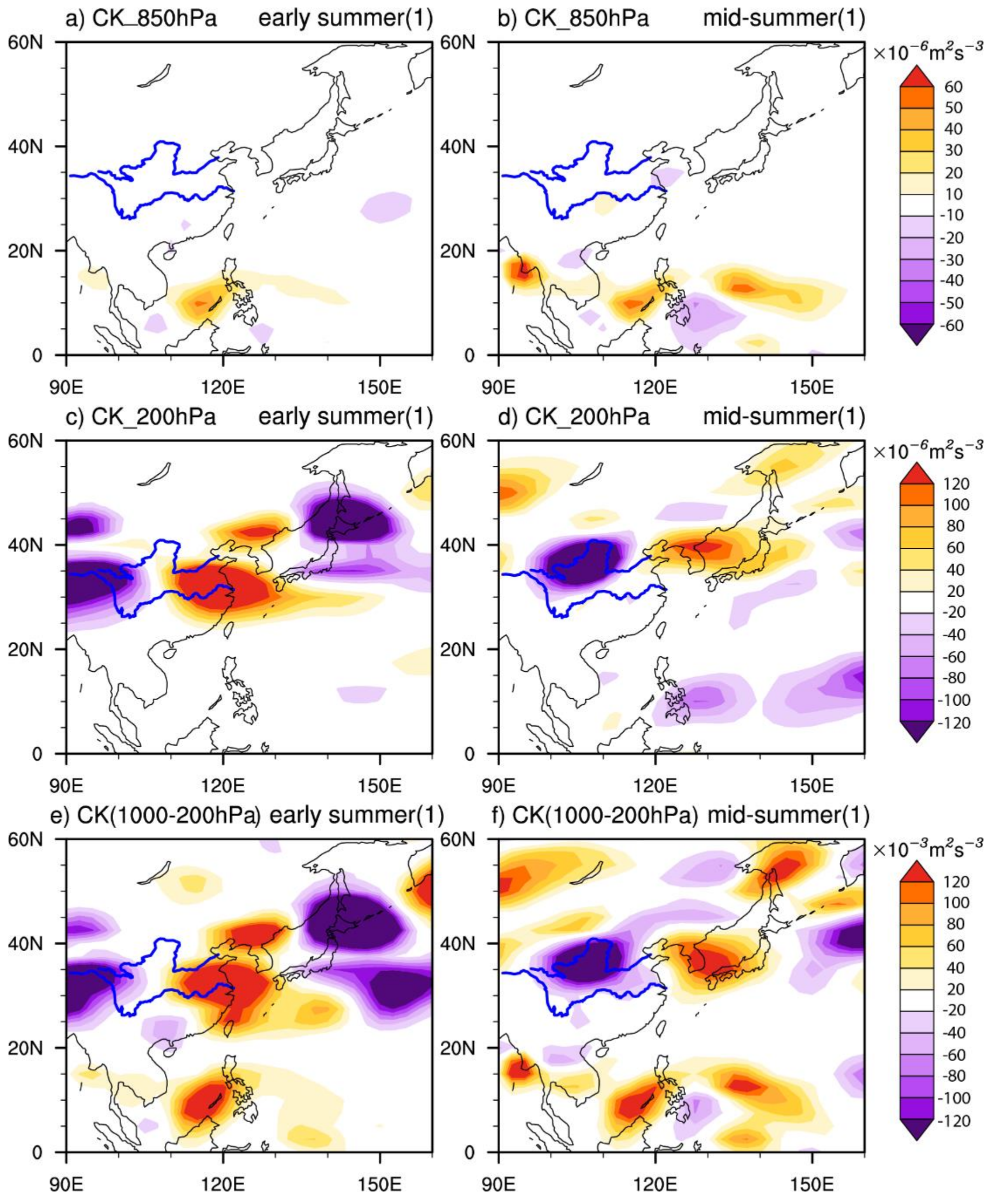

Figure 6. 850 hPa, 200 hPa and vertically integrated (1000–200 hPa) barotropic energy conversion *CK* during El Niño decaying early summer (a, c, e) and mid-summer (b, d, f).

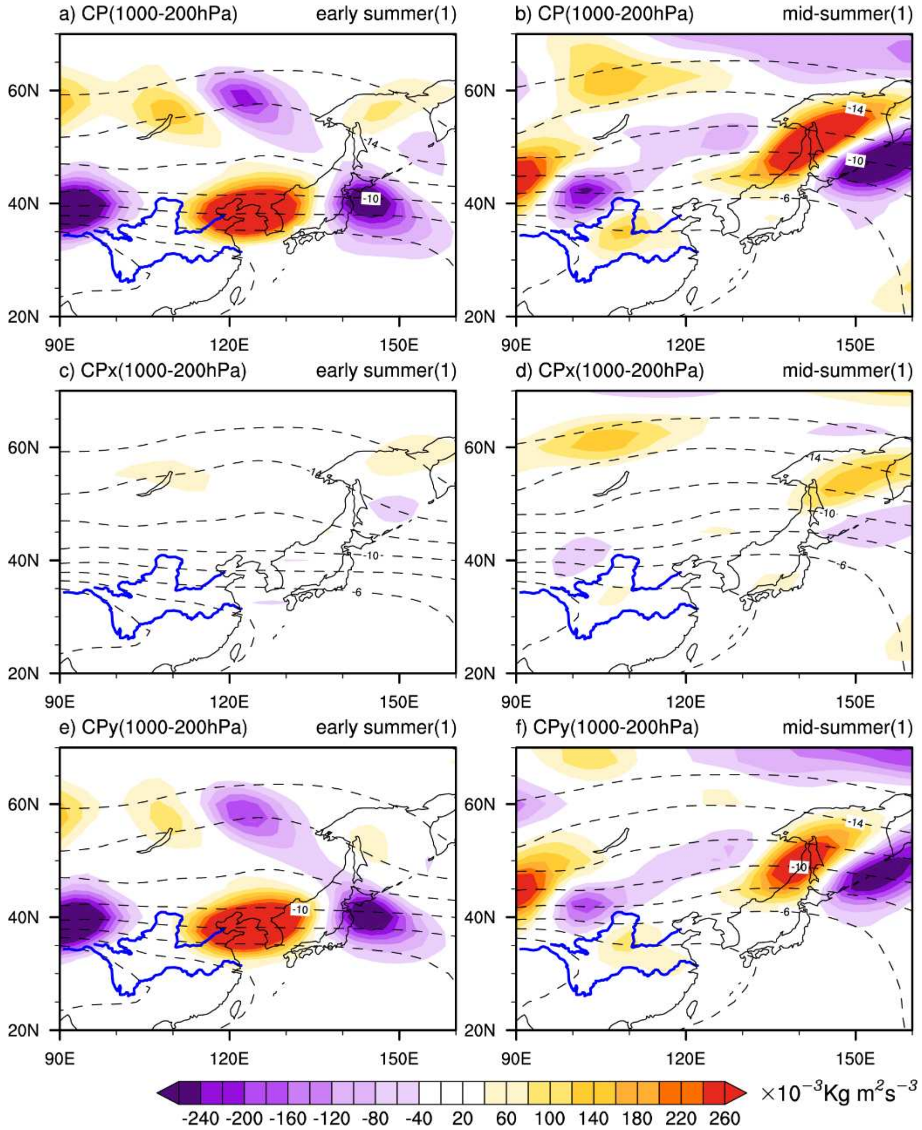

Figure 7. Vertically integrated (1000–200 hPa) baroclinic energy conversion CP ($\times\ 10^{-3} Kg \cdot m^2 \cdot s^{-3}$, colors) and climatological mean temperature at 500 hPa (°C, contours for -16, -14, -12, -10, -8, -6, -4, -2) during El Niño decaying early summer (a) and mid-summer (b). Also shown are CP_x and CP_y in the Eq. (2) during El Niño decaying early summer (c, e) and mid-summer (d, f).

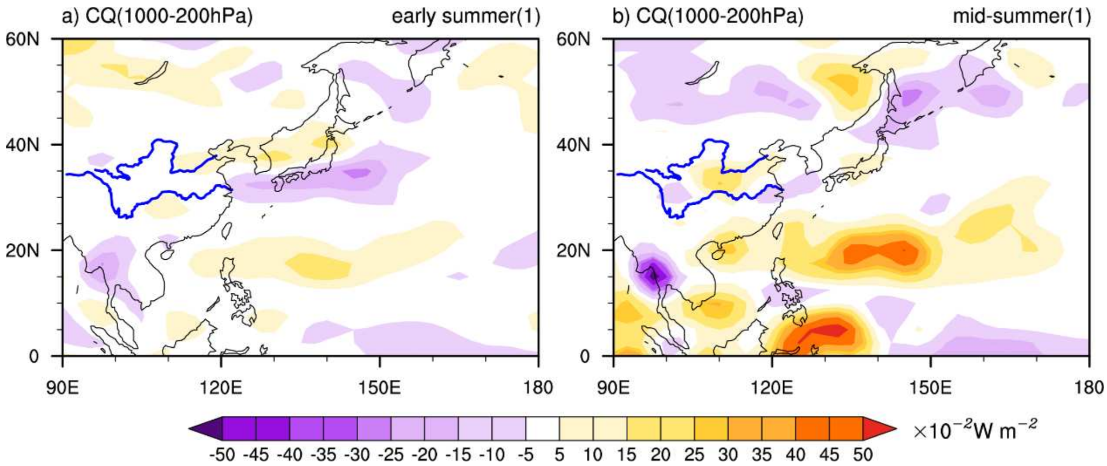

Figure 8. Vertically integrated (1000–200 hPa) diabatic energy generation CQ ($\times 10^{-2} W \cdot m^{-2}$, colors) during El Niño decaying early summer (a) and mid-summer (b).

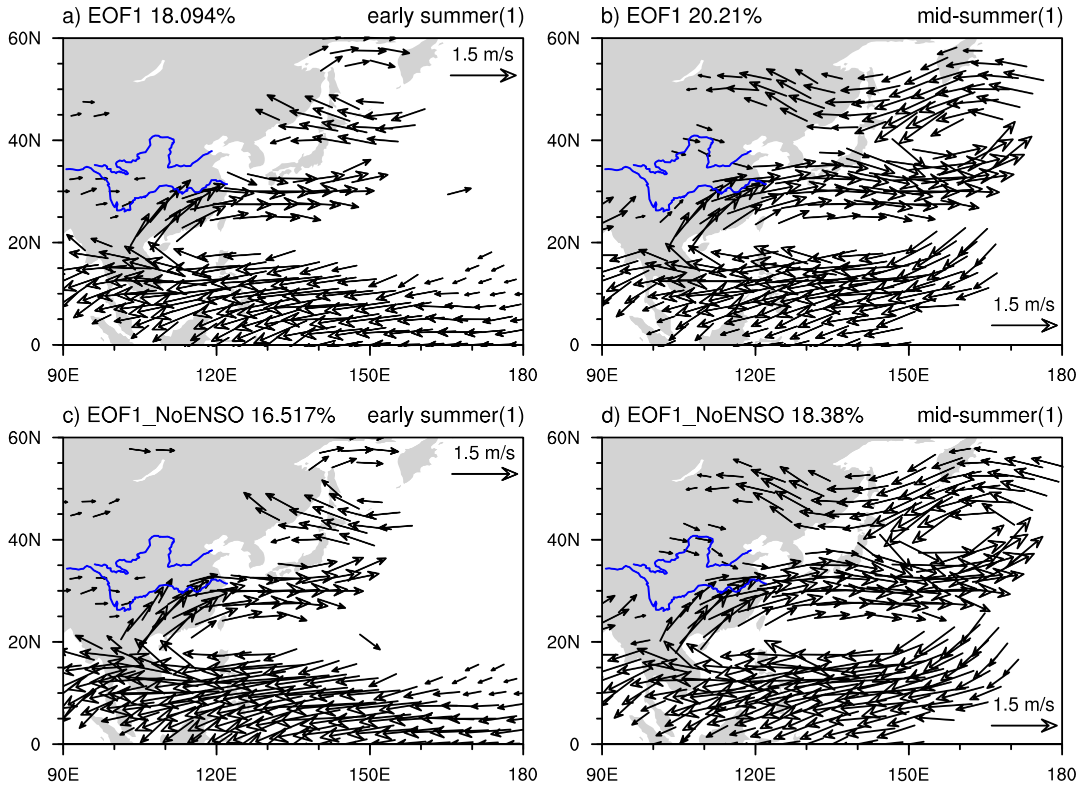

Figure 9. 850 hPa wind anomalies (vectors) regressed against standardized PC1 of the EOF analyses performed on standardized 850 hPa vorticity anomalies over the EA–NWP (10°–60°N, 100°–160°E) during El Niño decaying early summer (a) and mid-summer (b). c (d) is the same as a (b) but on the 850 hPa vorticity anomalies independent of ENSO. Vectors only exceeding the 90% confidence level are shown.

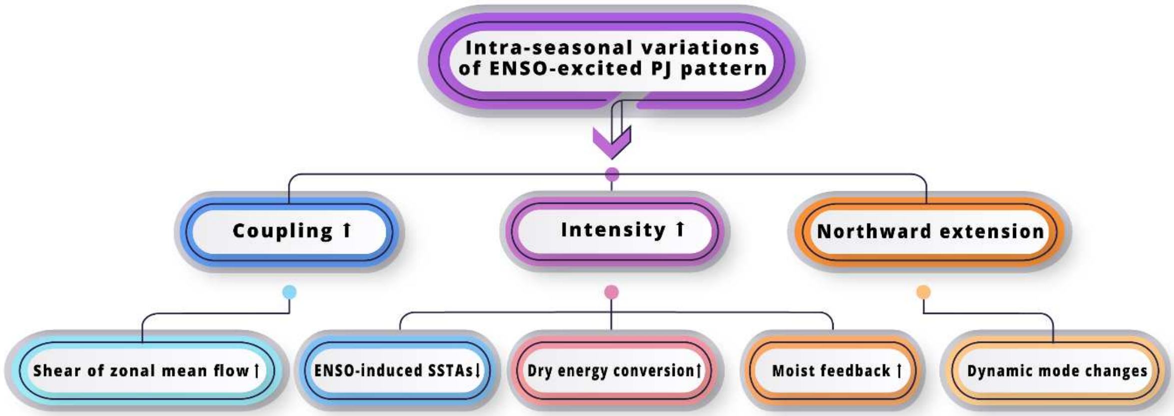

Figure 10. Schematic diagram illustrating the intra-seasonal variations of ENSO-excited PJ pattern during ENSO decaying summer.